

---

# V2X-M2C: Efficient Multi-Module Collaborative Perception with Two Connections

---

Hyunchul Bae Minhee Kang Heejin Ahn\*  
Korea Advanced Institute of Science and Technology (KAIST)  
{bhc2675, ministop, heejin.ahn}@kaist.ac.kr

## Abstract

In this paper, we investigate improving the perception performance of autonomous vehicles through communication with other vehicles and road infrastructures. To this end, we introduce a collaborative perception model **V2X-M2C**, consisting of multiple modules, each generating inter-agent complementary information, spatial global context, and spatial local information. Inspired by the question of why most existing architectures are sequential, we analyze both the *sequential* and *parallel* connections of the modules. The sequential connection synergizes the modules, whereas the parallel connection independently improves each module. Extensive experiments demonstrate that V2X-M2C achieves state-of-the-art perception performance, increasing the detection accuracy by 8.00% to 10.87% and decreasing the FLOPs by 42.81% to 52.64%.

## 1 Introduction

One of the fundamental components of autonomous vehicles (AVs) is the ability to perceive various driving environments. With the advance of deep learning, perception systems of AVs have demonstrated effectiveness in various studies, including object detection [1, 14, 22] and segmentation [1, 23, 24]. However, the perception of a single vehicle alone still has limitations caused by occlusion and limited sensor range.

To overcome these, multi-agent collaborative perception has been pivotal in enhancing perception across various environments. In particular, V2X (Vehicle-to-Everything) communications have enabled collaborative perception among heterogeneous agents such as vehicles and road infrastructure. Recognized methodologies such as CoBEVT [1], V2X-ViT [2], and Where2comm [3] have significantly improved the performance of 3D object detection.

The ongoing evolution of V2X collaborative perception necessitates continuous improvements. In particular, we develop an efficient model with manageable sizes and parameters. Consequently, our model can be implemented in lightweight hardware, becoming a more practical approach to collaborative perception. In addition, we propose a completely new concept for processing multi-agent features in collaborative perception. We have observed that most collaborative perception methods process multi-agent features *sequentially*. Because the sequential architecture handles the features as a whole and does not consider the individual features, it cannot always achieve the desired performance. By introducing and analyzing a *parallel* architecture, we open up new promising architecture directions in collaborative perception.

In this paper, we introduce V2X-M2C (V2X-Multi Modules with Two Connections), a framework designed to elevate effectiveness and efficiency based on parallel and sequential connections. Figure 2 illustrates two connections within holistic architecture, and Figure 3 depicts three key sub-modules: i) agent-wise attention module (A-Att) with heterogeneous relative pose encoding (HRPE) that interprets

---

\*Corresponding author.

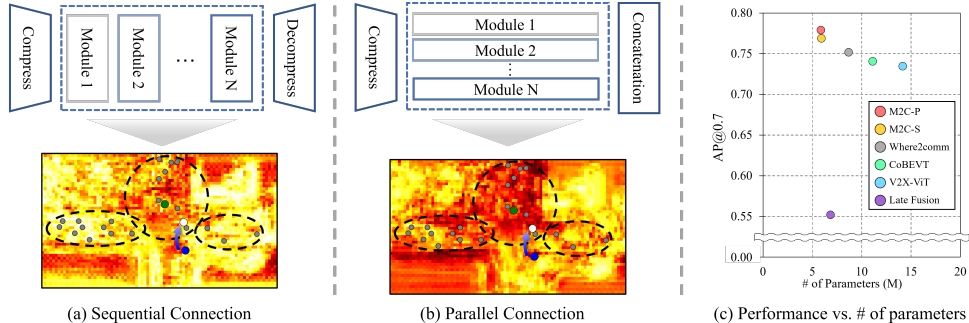


Figure 1: **About this paper.** (a) and (b) present two connections, and the attention weight resulted in M2C-S and M2C-P (details in Section 4.3). (c) V2X-M2C holds state-of-the-art performance with a reduced number of model parameters (details in Section 4.2)

interactions between multiple agents; ii) spatial-wise attention module (S-Att) that captures per-agent spatial global context; iii) heterogeneity-reflected convolution module (H-Conv) that generates spatial local information depending on agent types. We summarize our contributions as follows.

- We propose the collaborative perception model, **V2X-M2C** for 3D object detection. V2X-M2C is divided into two models: M2C-S connects the sub-modules in series, and M2C-P connects them in parallel. We consider multiple heterogeneous agents, making our model expandable to V2X scenarios. Our two models achieve state-of-the-art effectiveness, efficiency, and robustness to noise.
- We perform the qualitative comparison between the two connection types regarding how each sub-module influences the others. (Section 4.3)
- We utilize a channel compression layer (CCL) to make the overall fusion module lightweight, thereby significantly enhancing model efficiency while maintaining performance.
- We design a heterogeneity-reflected convolution module (H-Conv) to consider multiple heterogeneous agents with a low number of parameters and low computation complexity.

## 2 Related Work

**Collaborative Perception.** Intermediate fusion is the main technique that enables collaborative perception, which balances performance and communication demands. Previous studies obtain and share information using knowledge distillation [6], multi-module [1, 2, 5], and spatial confidence-aware communication [3]. They have proven effective in modeling heterogeneous data. However, their potential to reduce computational complexity and capture local context remains understudied. In this paper, we design the two different connection models using multi-modules to ensure model efficiency while outperforming the previous methods.

**Computer vision.** The introduction of the convolution layer has revolutionized computer vision; for example, AlexNet [7], VggNet [8], ResNet [9], etc. The convolution layer effectively captures local features while requiring fewer parameters than a fully connected layer. However, the convolution layer has difficulty capturing the relationships between distant features. The Vision Transformer (ViT) [10] leverages self-attention mechanisms to capture such global relationships effectively, yet at high computation complexity and with the challenge of maintaining translation equivariance. Several approaches, such as Swin Transformer [11], Pooling-based Vision Transformer [12], Neighborhood Attention Transformer [13], have been introduced to solve these challenges. Similar to these approaches, our approach takes full advantage of convolution and transformer to capture local information and global context, respectively.

## 3 Method

The overall architecture of V2X-M2C is shown in Figure 2. Depending on the connection type, the input of the sub-modules and the overall process differ. To distinguish it, we use  $\text{Conn.} \in \{\text{S}, \text{P}\}$ , where **S** indicates the M2C-S and **P** the M2C-P. In this section, we introduce the five main

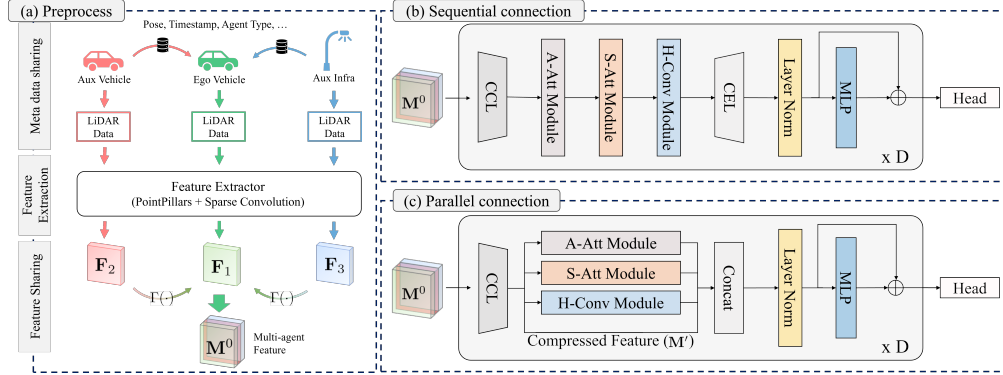


Figure 2: **Overview of our proposed collaborative perception system.** Our model consists of five steps: metadata sharing, feature extraction, feature sharing, fusion module, and detection head. The details of each component are discussed in Section 3. (a) shows preprocessing, (b) and (c) depict M2C-S and M2C-P fusion of multi-modules.

components: 1) metadata sharing, 2) feature extraction, 3) feature sharing, 4) fusion module, and 5) detection head.

### 3.1 Metadata sharing

The *ego agent* is the center agent that performs the object detection tasks, and the *aux agents* are auxiliary agents communicating to the ego agent. Let the number of connected agents, including the ego agent, be  $L$ , and the ego vehicle always has an index of 1. At metadata sharing, each  $l$ -th aux agent for  $l \in \{2, \dots, L\}$  sends their agent type  $t_l \in \{I, V\}$ , timestamp, and pose to the ego agent. Here, the agent type I refers to an infrastructure and V to a vehicle.

### 3.2 Feature Extraction

Our proposed model is based on intermediate fusion, which shares features extracted from raw point-cloud data. In V2X-M2C, the feature extraction mainly consists of 1) PointPillars and 2) Sparse Resnet Backbone.

**PointPillars.** PointPillars[14] splits point clouds into vertical columns. This enables PointPillars to use less memory and become faster than other voxel-based approaches, such as [15]. Also, the results of PointPillars are 2D pseudo-images. Thus, it is proper to apply a 2D convolution layer. To achieve efficient extraction, we employ PointPillars to convert point clouds of all agents to 2D pseudo-images.

**Sparse Resnet Backbone.** Sparsity is an important property of point clouds. The works [16, 25] suggest sub-manifold sparse convolution and sparse convolution, both of which are more effective and efficient for extracting features from sparse data. They extract feature  $F_l \in \mathbb{R}^{H \times W \times C}$  from the  $l$ -th agent's 2D pseudo-image where  $H$  is the height,  $W$  the width, and  $C$  the channels. All agents use the same backbone parameters. We deploy the Sparse Resnet (SpRes) backbone [28–30], which reduces memory usage and works more effectively than conventional dense convolution.

### 3.3 Feature Sharing

The ego agent receives the aux agents' features through communication. The features are first compressed to satisfy communication bandwidth and latency. Then, the ego agent receives the compressed features, decompresses them, transforms them into the ego agent coordinate, crops unnecessary information, and compensates for the time delay.

**Compression and Decompression.** For feature compression, all agents use the same encoder and decoder parameters. After an aux agent compresses its feature and sends it to the ego agent, the ego agent restores the feature using the decoder. We design an encoder and a decoder as a  $3 \times 3$  convolution layer to compress the channel size depending on the compression ratio  $N$ . The compressed feature

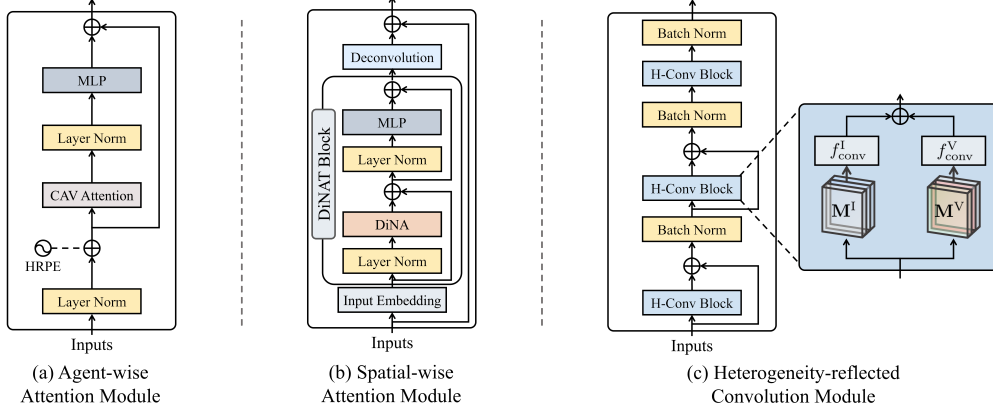


Figure 3: **Sub-modules in V2X-M2C.** (a) Agent-wise Attention (A-Att) sub-module with HRPE. (b) Spatial-wise Attention (S-Att) sub-module. (c) Heterogeneity-reflected Convolution (H-Conv) sub-module discussed in Sec. 3.4.

$\mathbf{F}'_l \in \mathbb{R}^{H \times W \times (C/N)}$  and decompressed feature  $\bar{\mathbf{F}}_l \in \mathbb{R}^{H \times W \times C}$  are determined by

$$\begin{aligned} \mathbf{F}'_l &= f_{\text{encoder}}(\mathbf{F}_l), \quad l = 1, \dots, L \\ \bar{\mathbf{F}}_l &= f_{\text{decoder}}(\mathbf{F}'_l), \quad l = 1, \dots, L. \end{aligned}$$

**Transformation.** The ego agent transforms the decoded features into the ego agent coordinate. Also, features outside the detection range are cropped to delete unnecessary information. After this process, we use a spatial-temporal correction module (STCM) [2] to compensate for the time delay caused by communication latency. We denote by  $\Gamma(\cdot)$  the sequential process of transform, crop, and STCM. By concatenating  $\Gamma(\bar{\mathbf{F}}_l)$  along the agent dimension, the multi-agent feature  $\mathbf{M}^0 \in \mathbb{R}^{L \times H \times W \times C}$  is generated. That is,

$$\mathbf{M}^0 = \parallel_{l \in [1, L]} \Gamma(\bar{\mathbf{F}}_l)$$

where  $\parallel_l(\cdot)$  denote the concatenation along the agent dimension.

### 3.4 Fusion Module

Our fusion module in V2X-M2C mainly consists of three sub-modules: agent-wise attention (A-Att), spatial-wise attention (S-Att), and heterogeneity-reflected convolution (H-Conv). Each sub-module generates inter-agent complementary information, spatial global context, and spatially detailed information, respectively. We refer to these as the *intent* of each sub-module. To prevent the model from being too heavy due to two transformer sub-modules (A-Att, S-Att), we use a channel-wise compression layer (CCL) to reduce the input feature size. This is one of the key components that makes our model efficient while maintaining state-of-the-art performance. Also, we propose two different module connections, *sequential* and *parallel*.

**Channel Compression Layer (CCL).** To reduce the input feature size in a simple and information-maintained manner, we design CCL as one fully connected (FC) layer that compresses the feature channel-wise. The input to the fusion module is the multi-agent feature  $\mathbf{M}^0$ , and the input at the  $d$ -th depth is  $\mathbf{M}^d \in \mathbb{R}^{L \times H \times W \times C}$ ,  $d = 1, \dots, D - 1$  where  $D$  is the maximum depth of the fusion module. Then, the output  $\mathbf{M}'$  of CCL at the  $d$ -th depth for each  $d = 0, \dots, D - 1$  is given by

$$\mathbf{M}' = f_{\text{CCL}}(\mathbf{M}^d) \in \mathbb{R}^{L \times H \times W \times C/4}.$$

CCL plays two roles in M2C-P. First, M2C-P generates the output by concatenating four intents along the channel. CCL compresses the feature channel size from  $C$  to  $C/4$  to match the input and output size. Second, from the second depth of the fusion module, CCL fuses the input feature channel-wise, and CCL actively improves the deficiency of each intent by adopting the strength of the others.

**Heterogeneous Relative Pose Encoding (HRPE).** Several factors, such as 1) agent type, 2) relative angle, and 3) distance, affect the point-cloud distribution and, therefore, change the feature distribution. HRPE offers these three pieces of information to consider the inter-agent relationship.

According to the  $l$ -th agent type  $t_l \in \{\text{I}, \text{V}\}$ , we define the period  $w_j$  as the inverse of the constant hyperparameter  $\tau \in \mathbb{R}$  to some powers of integer  $j \in [0, C/16 - 1]$ . In particular,

$$\omega_j = \begin{cases} 1/(\tau^{2j+1}), & t_l = \text{I} \\ 1/(\tau^{2j}), & t_l = \text{V}. \end{cases}$$

Using the approach in [26], we make fixed initialized encoding values  $\mathbf{p} \in \mathbb{R}^{C/4}$  of the relative angle  $\theta$  and distance  $d$  between the ego and aux agents as

$$\mathbf{p}[4j : 4(j+1)] = [\sin(d * \omega_j), \cos(d * \omega_j), \sin(\theta * \omega_j), \cos(\theta * \omega_j)],$$

where  $*$  is the multiplication.

After the initialization, the fixed encoding value passes the linear projection  $f_{\text{I}}$  or  $f_{\text{V}}$  depending on the agent type. It is added to the  $l$ -th compressed input feature  $\mathbf{M}'_l \in \mathbb{R}^{H \times W \times C/4}$ , and then, the encoded feature  $\mathbf{M}^{\text{pos}}$  concatenates the added feature along the agent dimension. That is,

$$\mathbf{M}^{\text{pos}} = \parallel_{l \in [1, L]} (\mathbf{M}'_l + f_{t_l}(\mathbf{p})).$$

**Agent-wise Attention Module (A-Att).** We use the vanilla attention module available in the code of [2], which we denote by  $\text{CAV\_ATT}^d$  at the  $d$ -th depth. This module does not distinguish agent type and utilizes a multi-head self-attention transformer. For each connection  $\text{Conn.}$ , the output  $\text{Conn.}\mathbf{M}^{\text{AA}}$  of A-Att at the  $d$ -th depth is given by

$$\text{Conn.}\mathbf{M}^{\text{AA}} = \begin{cases} \text{CAV\_ATT}^1(\mathbf{M}^{\text{pos}}) + \mathbf{M}', & d = 1 \\ \text{CAV\_ATT}^d(\mathbf{M}') + \mathbf{M}', & d \neq 1. \end{cases}$$

We use HRPE in the first depth of the fusion module to better interpret the other agent features.

**Spatial-wise Attention Module (S-Att).** We use Dilated Neighborhood Attention Transformer (DiNAT)[17] to interpret a global context. DiNAT maintains translation equivariance and reduces computation burden by resembling the convolution operation. Also, it efficiently widens the receptive fields by using the dilation rate. We use one block of the original DiNAT module and make it lighter to enhance the overall efficiency of the model. The output  $\text{Conn.}\mathbf{M}^{\text{SA}}$  of S-Att is determined by

$$\begin{aligned} \text{S}\mathbf{M}^{\text{SA}} &= \text{DiNAT}(\text{S}\mathbf{M}^{\text{AA}}) + \text{S}\mathbf{M}^{\text{AA}}, \\ \text{P}\mathbf{M}^{\text{SA}} &= \text{DiNAT}(\mathbf{M}') + \mathbf{M}'. \end{aligned}$$

**Heterogeneity-reflected Convolution Module (H-Conv).** To consider multiple heterogeneous agents, most prior works use transformer-based approaches [2, 32, 33]. On the other hand, we use convolution layers to handle multiple heterogeneous agents and prevent our model from being computationally heavy. H-Conv uses two pipelines, which have the same architecture but are distinguished by agent types. Each pipeline has two convolution layers with residual connections. In each pipeline, the  $l$ -th agent input feature to H-Conv is first divided into  $\text{Conn.}\mathbf{M}^{\text{I}}_l$  and  $\text{Conn.}\mathbf{M}^{\text{V}}_l$  depending on the agent types. Then, these are concatenated along the agent dimension, generating  $\text{Conn.}\mathbf{M}^{\text{I}} (\text{Conn.}\mathbf{M}^{\text{V}})$ . Then,  $\text{Conn.}\mathbf{M}^{\text{I}} (\text{Conn.}\mathbf{M}^{\text{V}})$  is passed through the convolution operation  $f_{\text{conv}}^{\text{I}}(\cdot) (f_{\text{conv}}^{\text{V}}(\cdot))$ . The output  $\text{Conn.}\mathbf{M}^{\text{HC}}$  of H-Conv is determined by

$$\text{Conn.}\mathbf{M}^{\text{HC}} = f_{\text{conv}}^{\text{I}}(\text{Conn.}\mathbf{M}^{\text{I}}) + f_{\text{conv}}^{\text{V}}(\text{Conn.}\mathbf{M}^{\text{V}})$$

where

$$\begin{aligned} \text{Conn.}\mathbf{M}^{\text{I}} &= \parallel_{l \in [1, L]} \text{Conn.}\mathbf{M}^{\text{I}}_l, & \text{Conn.}\mathbf{M}^{\text{V}} &= \parallel_{l \in [1, L]} \text{Conn.}\mathbf{M}^{\text{V}}_l \\ \text{S}\mathbf{M}^t_l &= \begin{cases} \text{S}\mathbf{M}^{\text{SA}}_l, & t = t_l \\ 0, & t \neq t_l \end{cases}, & \text{P}\mathbf{M}^t_l &= \begin{cases} \mathbf{M}'_l, & t = t_l \\ 0, & t \neq t_l. \end{cases} \end{aligned}$$

**Sequential/Parallel Connection (M2C-S/M2C-P).** M2C-S puts the three sub-modules (A-Att, S-Att, and H-Conv) in series and, at the end, uses the channel expand layer (CEL),  $f_{\text{CEL}} : \mathbb{R}^{C/4} \rightarrow \mathbb{R}^C$ , to restore the original channel size of  $C$ . M2C-P concatenates the intents of the three sub-modules and

the compressed original feature  $M'$ . Then, the output of  $d$ -th depth fusion module  $M^d$  is generated by applying a multilayer perceptron (MLP) with the residual connection. That is,

$$M^d = \text{MLP}(M^O) + M^O, \quad d = 1, \dots, D$$

where

$$M^O = \begin{cases} f_{\text{CEL}}(\text{SM}^{\text{HC}}), & \text{Conn.} = \text{S} \\ \text{PM}^{\text{AA}} \parallel \text{PM}^{\text{SA}} \parallel \text{PM}^{\text{HC}} \parallel M', & \text{Conn.} = \text{P}. \end{cases}$$

Depending on the connection type, the learning tendency of the sub-modules is different. The property of M2C-S is that the input of one sub-module is the output of the other. This dependency makes the sub-modules learn to enhance their performance as a whole. M2C-P concatenates all the intents and applies MLP. Then, the output  $M^d$  is applied to the  $(d + 1)$ -th depth fusion module as the input feature. The FC layers in MLP and CCL learn to emphasize the strength of each intent to compensate for the deficiency of the others. In other words, the sub-modules learn to strengthen what they do best to generate rich information for detection. Our detailed analysis of these learning tendencies is presented in Section 4.3.

### 3.5 Head

After passing the last depth, we get the final output  $M^D$ . We extract the ego agent output  $M_1^D$  and apply two  $1 \times 1$  convolution layers,  $f_{\text{head}}^{\text{cls}}(\cdot)$  and  $f_{\text{head}}^{\text{reg}}(\cdot)$ , for the detection box classification and regression, respectively. Specifically,  $f_{\text{head}}^{\text{cls}}(\cdot)$  makes the classification output tensor  $\hat{Y}_{\text{cls}} \in \mathbb{R}^{H \times W \times 2}$  that identifies whether an object is a vehicle or not, and  $f_{\text{head}}^{\text{reg}}(\cdot)$  makes the regression output tensor  $\hat{Y}_{\text{reg}} \in \mathbb{R}^{H \times W \times 14}$  that contains center of boxes  $(x, y, z)$ , size of boxes  $(w, l, h)$  and heading of vehicle  $\phi$ . We use the total loss  $\mathcal{L}_{\text{total}} = \mathcal{L}_{\text{cls}} + \mathcal{L}_{\text{reg}}$  where  $\mathcal{L}_{\text{cls}}$  is calculated using  $\hat{Y}_{\text{cls}}$  and focal loss [27] and  $\mathcal{L}_{\text{reg}}$  is calculated using  $\hat{Y}_{\text{reg}}$  and the smooth L1 loss [31].

## 4 Experiments

### 4.1 Experimental Settings.

**Comparison Models and Datasets.** We compare our proposed architecture with state-of-the-art (SOTA) models [1], [2], [3] on the V2XSet [2] and OPV2V [18] datasets to validate performance in both the V2V (Vehicle-to-Vehicle) and V2X scenarios. V2XSet is a simulated dataset, including V2X scenarios, co-simulated using CARLA [19] and OpenCDA [20]. OPV2V is a simulated dataset, only including V2V scenarios. We set the LiDAR detection range as  $x \in [-140.8, 140.8]$  and  $y \in [-38.4, 38.4]$ . A detailed description of the datasets and models is in Appendix B.1 and B.2.

**Evaluation Metrics and Noise Settings.** We calculate the Average Precision (AP) at the Intersection-over-Union (IoU) thresholds of 0.5 and 0.7 to evaluate 3D detection accuracy and use a number of parameters (# Params) and GFLOPs to compare model efficiency. To compare models for various situations, we add noise to training and inference data, which includes latency, localization, and heading noises. The latency  $t_{\text{lag}}$  is divided into constant or random, and the random  $t_{\text{lag}}$  is based on the total time delay [2]. The localization and heading noises use normal distributions with standard deviations  $\sigma_{\text{loc}}$  and  $\sigma_{\text{hdg}}$ , respectively. We train models with three different noisy settings: perfect, simple noise, and harsh noise. The perfect setting does not apply any noise, and the simple noise setting applies constant  $t_{\text{lag}}$  of 100 ms, and the localization and heading noises with  $\sigma_{\text{loc}} = 0.2$  m and  $\sigma_{\text{hdg}} = 0.2^\circ$ . Detailed information about training and inference setting is described in Appendix B.4 and B.5.

### 4.2 Quantitative evaluation

**Detection Accuracy.** Table 1 compares the proposed V2X-M2C with the other SOTA methods. In particular, we consider single-agent detection (No Fusion), late fusion, CoBEVT [1], V2X-ViT [2], and Where2comm [3] (see detection visualization in Appendix C.2). We observe that: i) Compared with No Fusion, M2C-S/M2C-P enhances the accuracy by 42.70%/41.62% on V2XSet, and 51.94%/49.75% on OPV2V in the perfect setting. ii) In the perfect setting, M2C-S increases the

Table 1: Comparison of detection accuracy and model efficiency.

Model	Perfect		Simple Noise		# Params	GFLOPs
	V2XSet AP@0.5/0.7	OPV2V AP@0.5/0.7	V2XSet AP@0.5/0.7	OPV2V AP@0.5/0.7		
No Fusion	0.754 / 0.602	0.659 / 0.545	0.754 / 0.602	0.659 / 0.545	-	-
Late Fusion	0.885 / 0.764	0.852 / 0.768	0.844 / 0.552	0.821 / 0.597	6.58M	<b>25</b>
CoBEVT [1]	0.896 / 0.841	0.855 / 0.793	0.870 / 0.740	0.780 / 0.615	11.14M	213
V2X-ViT [2]	0.886 / 0.807	0.848 / 0.769	0.872 / 0.734	0.795 / 0.632	14.17M	287
Where2comm [3]	0.913 / 0.853	0.854 / 0.789	0.888 / 0.751	0.778 / 0.624	8.69M	177
M2C-S (Ours)	<b>0.922 / 0.860</b>	<b>0.887 / 0.828</b>	<b>0.907 / 0.769</b>	<b>0.844 / 0.682</b>	5.97M	103
M2C-P (Ours)	0.904 / 0.853	0.869 / 0.816	0.892 / <b>0.779</b>	0.828 / 0.681	<b>5.92M</b>	103

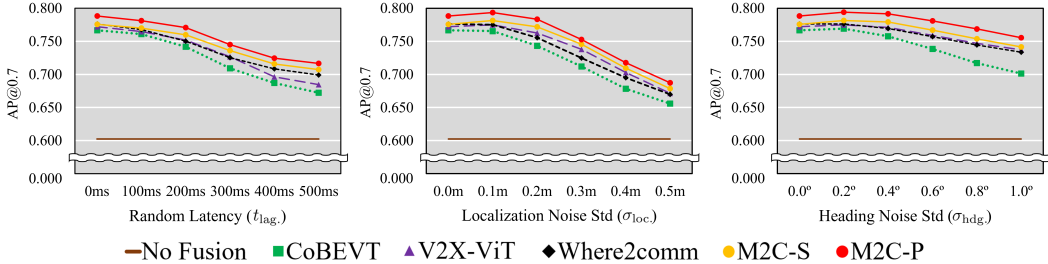


Figure 4: Robustness in various noise ranges.

accuracy by 0.77% compared with Where2comm on V2XSet and 4.49% compared with CoBEVT on OPV2V at AP@0.7. iii) In the simple noise setting, M2C-S/M2C-P increases the accuracy by 2.28%/3.63% compared with Where2comm on V2XSet, and 8.00%/7.79% compared with V2X-ViT on OPV2V at AP@0.7. Our proposed M2C-S and M2C-P outperform the SOTA models on both datasets regardless of noise.

**Model Efficiency.** Table 1 compares model efficiency in terms of # Params and GFLOPs. The # Params in M2C-S/M2C-P is reduced by 58.1%/58.4% compared with V2X-ViT and by 31.65%/32.22% compared with Where2comm [3]. The GFLOPs of M2C-S and M2C-P are reduced by 64.11% compared with V2X-ViT [2] and 41.80% compared with Where2comm [3]. Substantially, we find that our models have fewer parameters than the PoinPillars-based late fusion. This shows our models can work in lightweight hardware.

**Noise Robustness.** To evaluate the robustness to noises, we utilize models trained with a harsh noise setting. We apply various ranges of noise components: random  $t_{lag} \in [0 \text{ ms}, 500 \text{ ms}]$ ,  $\sigma_{loc} \in [0.0 \text{ m}, 0.5 \text{ m}]$ , and  $\sigma_{hdg} \in [0.0^\circ, 1.0^\circ]$  from the zero noise (0 ms, 0.0 m, 0.0°). As shown in Fig. 4, M2C-S and M2C-P outperform the SOTA models in all the noise components. At the same time, M2C-S and M2C-P show the lowest noise sensitivity among the SOTA models (Detailed values in Appendix C.1). For the severe noise setting (500 ms / 0.5 m / 1.0°), the rate of change (i.e., sensitivity) of M2C-S and M2C-P decreases by 8.82%/4.40%/12.52% and 9.07%/4.16%/12.79% from the zero noise, respectively, while that of V2X-ViT [2] decreases by 11.34%/4.54%/13.04% and that of Where2comm [3] decreases by 9.96%/5.51%/13.71%.

### 4.3 Qualitative Evaluation

**Visualization of CCL Weights.** In Figure 5, we visualize the weights of CCL in M2C-P that consist of four sections indicating A-Att, S-Att, H-conv, and original layers for identifying the tendency of learning. We observe that i) the weights of H-Conv show the highest values in the perfect and simple noise setting as the depth gets deeper. In particular, in the third depth, the sum of the weights of the H-Conv section is 482.498 in the perfect setting and 541.413 in the simple noise setting, while that of the other sections (A-Att / S-Att / Original) is 210.488 / 275.469 / 300.404 and 185.661 / 260.079 / 298.485, respectively. ii) Comparing the perfect to noise setting, the sum of the weights of the H-Conv section increases from 482.498 to 541.413, whereas the other sums decrease. It highlights that H-Conv plays a main role in compensating for the other intents and overcoming noise disturbance. This also contributes to the low noise sensitivity of our models discussed in Section 4.2.

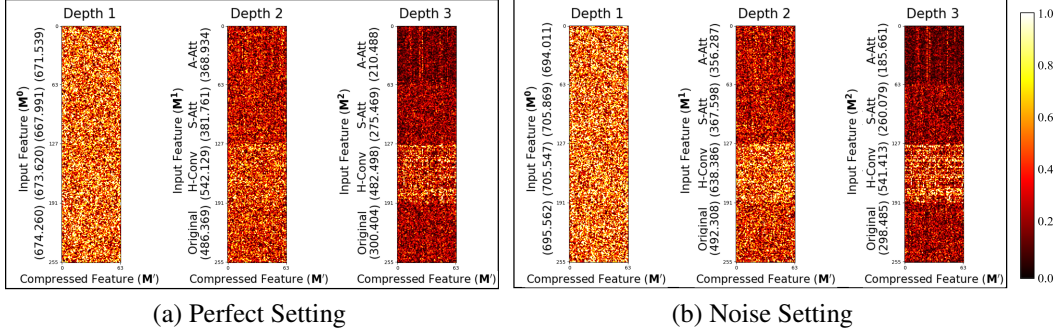


Figure 5: **Visualization of CCL weights in M2C-P with the perfect and noisy setting.** The weight matrix is divided into four sections (A-Att, S-Att, H-conv, original). The number in the parentheses of each section is the sum of the section’s weights.

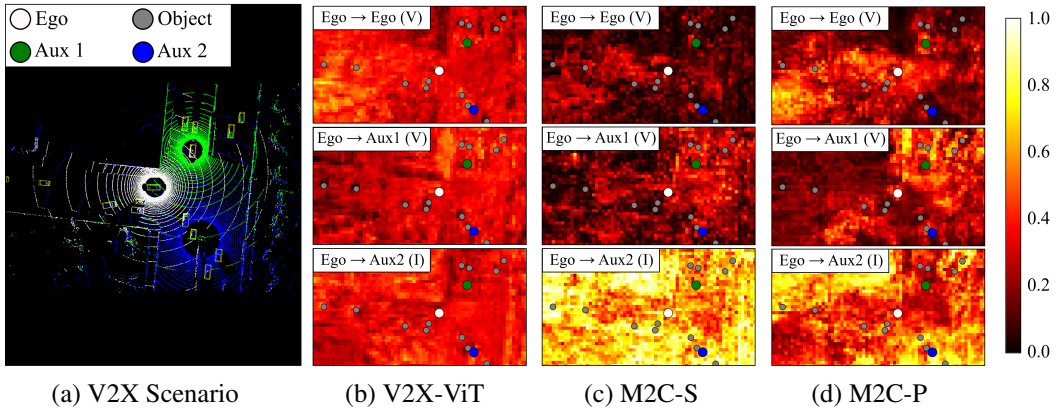


Figure 6: **Aggregated LiDAR points and attention map.** The white circle is the ego agent, and the blue and green circles are aux agents. Small grey circles are vehicles in the detection range.

**Visualization of Attention Weights.** In Figure 6, we visualize the attention weights in A-Att, where the brighter colors indicate the areas the ego agent focuses on. Some observations to notice are as follows: i) Our models show a clear difference between the regions that are paid attention to or not, compared to the V2X-ViT’s attention weights (Figure 6-(b)). ii) Our models have different attention tendencies. For M2C-P in Figure 6-(d), the ego agent relies on its own confidence regions where its point clouds are dense and not occluded. Also, it relies on the aux agent’s confidence regions to incorporate wide-range information. In M2C-S in Figure 6-(c), the ego agent focuses on the areas where objects densely exist. The tendencies are more explicitly identified in the infrastructure data, which has a wider detection range but is sparse and can be noisy at far distances. The ego agent in M2C-S leverages the infrastructure data heavily, simultaneously differentiating between roads and objects. On the other hand, the ego agent in M2C-P takes the infrastructure data relatively less because the infrastructure data has lower confidence than the data from nearby aux agents.

#### 4.4 Ablation Study.

**Effect of sub-modules.** We present the ablation study results in Table 2. The inter-agent complementary information, which is related to A-Att, affects both models significantly. In the perfect/simple noise setting, the performances of M2C-S decrease by 20.25%/12.47%, and that of M2C-P decreases by 18.09%/10.22% at AP@0.7 by eliminating A-Att. H-Conv also affects M2C-S and M2C-P, which decreases the performances by 2.78%/4.96% and 1.87%/4.22%, respectively.

**CCL compression ratio.** We train M2C-S with various compression rates in CCL to validate whether the reduction in feature size causes information loss. Table 3 shows that the rate of  $\times 2$  yields the best performance at AP@0.7. Although the performance of the rate of  $\times 4$  is lower by 2.24% compared with the rate of  $\times 2$  in the perfect and noisy settings, the number of parameters and GFLOPs are

Table 2: Effect of sub-modules in V2X-M2C

	A-Att	S-Att	H-Conv	Original	Perfect AP@0.5/0.7	Simple Noise AP@0.5/0.7
M2C-S		✓	✓	-	<b>0.805 / 0.684</b>	<b>0.809 / 0.683</b>
	✓		✓	-	0.910 / 0.851	0.899 / 0.768
	✓	✓	✓	-	<b>0.883 / 0.835</b>	<b>0.864 / 0.743</b>
M2C-P	✓	✓	✓	✓	<b>0.806 / 0.698</b>	<b>0.808 / 0.698</b>
	✓		✓	✓	0.893 / 0.849	0.883 / 0.764
	✓	✓	✓	✓	<b>0.883 / 0.836</b>	<b>0.863 / 0.745</b>
	✓	✓	✓	✓	0.898 / 0.847	0.893 / 0.776
	✓	✓	✓	✓	0.904 / 0.853	0.894 / 0.785

Table 3: Effect of comp. ratio at AP@0.7 in M2C-S. Noisy means the simple noise.

Rate	Perfect	Noisy	# Params	GFLOPs
×1	0.864	0.800	24.76M	790
×2	0.865	0.798	9.75M	230
×4 (Ours)	0.860	0.781	5.94M	103
×8	0.842	0.751	4.97M	74

Table 4: Ablation study of HRPE at AP@0.7. Noisy means the simple noise.

Model	HRPE	Perfect	Noisy
M2C-S	✓	0.860	0.781
		0.858	0.765
M2C-P	✓	0.853	0.785
		0.855	0.772

decreased by 39.1% and 55.22%, respectively. From the efficiency perspective, we select the rate of ×4 as the final setting.

**Effect of HRPE.** We use HRPE in A-Att to help the module understand the features of the other agents. Table 4 shows that HRPE significantly enhances the performance of the two models in the noise setting, while it does not contribute much in the perfect setting. The results show that HRPE, by setting the two hyperparameters  $\theta$  and  $d$  (given in Appendix B.3), makes our models robust to noise.

## 5 Conclusion

This paper has proposed efficient collaborative perception models, M2C-S and M2C-P, based on two different connection types. The two critical components that enhance the effectiveness and efficiency of our models are CCL and H-Conv. CCL reduces the feature size and makes our fusion module lightweight, and H-Conv handles multiple heterogeneous agents and simultaneously prevents our models from being computationally heavy. In addition, we have compared and analyzed M2C-S and M2C-P through extensive experiments regarding detection accuracy, noise robustness, and learning tendency. We envision these analyses providing important guidelines to design new model architectures for collaborative perception considering different connections of multiple features.

**Limitation and future work.** Although we have analyzed the characteristics of our two models and achieved the SOTA performances, we did not propose a single integrated model that shows superior performance in all aspects. In future work, we plan to integrate the parallel and sequential models into a single architecture and improve A-Att and S-Att along with the integration.

## A Our Contributions

- We propose the collaborative perception model, **V2X-M2C** for 3D object detection. V2X-M2C is divided into two models: M2C-S connects the sub-modules in series, and M2C-P connects them in parallel. We consider multiple heterogeneous agents, making our model expandable to V2X scenarios. Our two models achieve state-of-the-art (SOTA) effectiveness, efficiency, and robustness to noise.
- We perform the qualitative comparison between the two connection types in terms of how each sub-module influences the each other.
- We utilize a channel compression layer (CCL) to make the overall fusion module lightweight, thereby significantly enhancing model efficiency while maintaining performance.
- We design a heterogeneity-reflected convolution module (H-Conv) to consider multiple heterogeneous agents with a low number of parameters and low computation complexity.

## B Implementation Details

### B.1 Dataset.

We use the V2XSet [2] and OPV2V [18] datasets to train and validate models in both V2V and V2X scenarios.

**V2XSet.** V2XSet is a simulated dataset supporting V2X perception, co-simulated using CARLA [19] and OpenCDA [20]. It comprises 73 scenes with a minimum of 2 to 5 connected agents and includes 11K 3D annotated LiDAR point cloud frames. The training, validation, and testing sets consist of 6.7K, 2K, and 2.8K frames, respectively.

**OPV2V.** OPV2V is a simulated dataset designed for multi-agent V2V perception. Each frame typically comprises approximately 3 CAVs, with a minimum of 2 and a maximum of 7. It includes 10.9K LiDAR point cloud frames with 3D annotations. The training, validation, and testing splits include 6.8K, 2K, and 2.2K frames, respectively.

### B.2 Comparison Models.

We select comparison models through several considerations to check whether our models are significant and reliable: i) The model has been suggested within the past two years. ii) The model has been cited in many related works. iii) The model has distinct methods or characteristics from each other. Considering these factors, we select CoBEVT [1], V2X-ViT [2], and Where2comm [3]. Unlike other models, CoBEVT presents a framework for multi-agent multi-camera perception that collaboratively produces BEV map predictions using both camera and LiDAR. V2X-ViT attempts to utilize heterogeneous agents, such as vehicles and road infrastructure, and solve the problem of heterogeneity between them using a transformer with a graph structure. Where2comm introduces a spatial confidence map, enabling agents to share only spatially sparse yet perceptually important information.

### B.3 Hyperparameter Details.

**Training Parameters.** For a fair comparison, we train both our models and SOTA models using AdamW [21], with a learning rate of  $3e-4$  and a weight decay of 0.01. We use the same learning scheduler, Cosine Annealing Warm-Up Restarts [34], applying a warm-up learning rate of  $2e-4$  and warm-up epochs. We train the models for up to 40 epochs and use a maximum of five connected agents, including the ego agent. The models are trained and validated on an RTX 4090.

**Model Parameters.** Regarding the fusion module, HRPE in A-att utilizes the relative angle  $\theta$  and distance  $d$ . In M2C-S, the relative angle and distance are segmented into  $10^\circ$  and 30 m, respectively. In M2C-P, these are divided into  $10^\circ$  and 20 m. HRPE then uses the integer value rounded from the divided terms. In S-att, the lightweight DiNAT [17] features two depths. For DiNAT’s hyperparameters, we use a  $7 \times 7$  kernel with dilation rates of 4 and 2 applied to each depth, respectively. The H-conv comprises three blocks, each incorporating heterogeneity-reflected convolution using a  $3 \times 3$  kernel. The first and second blocks employ a residual connection linking each block’s input and output, while the third block does not.

#### B.4 Training Details.

We train the models in three different noise settings: 1) perfect setting, 2) simple noise setting, and 3) harsh noise setting. Each noise setting differs in the compression ratio for feature sharing and noise values ( $t_{\text{lag}}, \sigma_{\text{loc}}, \sigma_{\text{hdg}}$ ).

**Perfect Setting.** Models are trained up to 40 epochs, and the detailed configuration is as follows.

- Compression Ratio:  $\times 32$
- Noise Value: (0 ms,  $0.0^\circ$ , 0.0 m)

**Simple Noise Setting.** Models are trained up to 40 epochs, and the detailed configuration is as follows.

- Compression Ratio:  $\times 32$
- Noise Value: (constant 100 ms,  $0.2^\circ$ , 0.2 m)

**Harsh Noise Setting.** Training in the harsh noise setting consists of three steps: 1) perfect setting training, 2) compressed setting fine-tuning, and 3) noise setting fine-tuning.

The perfect setting training trains the models up to 40 epochs with the configurations below.

- Compression Ratio:  $\times 1$  (not compressed)
- Noise Value: (0 ms,  $0.0^\circ$ , 0.0 m)

After completing the perfect setting training, we select the model with the best performance weight from the 31st to 40th epoch at AP@0.7. Then, we train the model for an additional two epochs. At this step, we convert the compression ratio from  $\times 1$  to  $\times 32$ . Finally, we train the model for an additional thirty-eight epochs with the noise settings as below.

- Compression Ratio:  $\times 32$
- Noise Value: (random 200 ms,  $0.2^\circ$ , 0.2 m)

#### B.5 Inference Details.

The results of training differ even when the model has the same architecture and hyperparameters due to the properties of gradient descent. Additionally, the random seed influences the probability distribution, and this distribution affects the difficulty level of scenarios. To ensure model reliability, we evaluate models through several inferences depending on the noise setting: 1) perfect setting, 2) simple noise setting, and 3) harsh noise setting.

**Perfect Setting.** In the perfect setting, we utilize three different pre-trained models that have been trained under this setting. We evaluate each model’s performance by averaging the AP@0.5/0.7 of thirty weights that are derived from the pre-trained models during the 31st to 40th epochs.

**Simple Noise Setting.** Regarding the simple noise setting, we consider noise variations by seed. We used nine models pre-trained under the simple noise setting, applying three different seeds (25, 26, and 27). The process is the same as in the perfect setting, except for evaluating the performance of the ablation study. For the ablation study’s performance evaluation, we simplify the process by only applying seed 27. We use seed 27 because its performance demonstrates typical results upon observation; seed 25 results in easy noise, and seed 26 in hard noise.

**Harsh Noise Setting.** To evaluate noise robustness, we use models pre-trained with harsh noise settings under three seeds (25, 26, and 27). We calculate AP@0.5/0.7 depending on three harsh noise components: random latency, localization, and heading noise standard deviation. We create sixteen noise sets by varying one component while setting the others to zero: random  $t_{\text{lag}} \in [0 \text{ ms}, 500 \text{ ms}]$ ,  $\sigma_{\text{loc}} \in [0.0 \text{ m}, 0.5 \text{ m}]$ , and  $\sigma_{\text{hdg}} \in [0.0^\circ, 1.0^\circ]$ , including the zero noise scenario (0 ms, 0.0 m,  $0.0^\circ$ ). We use the weight from the pre-trained model results from the 36th to 40th epochs and calculate AP@0.5/0.7 for each weight depending on each noise set. Finally, we evaluate the performance by averaging AP@0.5/0.7 for each noise set.

Table 5: Robustness to various ranges of noises with detailed values.

Model	Random Latency ( $t_{\text{lag.}}$ )					
	0 ms	100 ms	200 ms	300 ms	400 ms	500 ms
CoBEVT [1]	0.767	0.761	0.742	0.709	0.687	0.672
V2X-ViT [2]	0.772	0.765	0.752	0.727	0.696	0.685
Where2comm [3]	0.776	0.768	0.750	0.725	0.708	0.699
M2C-S (Ours)	0.776	0.770	0.760	0.736	0.716	0.707
M2C-P (Ours)	<b>0.788</b>	<b>0.781</b>	<b>0.771</b>	<b>0.745</b>	<b>0.725</b>	<b>0.717</b>
Model	Location Noise std. ( $\sigma_{\text{loc.}}$ )					
	0.0 m	0.1 m	0.2 m	0.3 m	0.4 m	0.5 m
CoBEVT [1]	0.767	0.765	0.743	0.712	0.678	0.656
V2X-ViT [2]	0.772	0.775	0.763	0.738	0.703	0.671
Where2comm [3]	0.776	0.775	0.755	0.725	0.695	0.670
M2C-S (Ours)	0.776	0.781	0.772	0.746	0.710	0.679
M2C-P (Ours)	<b>0.788</b>	<b>0.793</b>	<b>0.783</b>	<b>0.753</b>	<b>0.718</b>	<b>0.687</b>
Model	Heading Error std. ( $\sigma_{\text{hdg.}}$ )					
	0.0°	0.2°	0.4°	0.6°	0.8°	1.0°
CoBEVT [1]	0.767	0.769	0.758	0.738	0.717	0.701
V2X-ViT [2]	0.772	0.775	0.771	0.759	0.747	0.737
Where2comm [3]	0.776	0.776	0.769	0.757	0.745	0.733
M2C-S (Ours)	0.776	0.781	0.779	0.767	0.754	0.742
M2C-P (Ours)	<b>0.788</b>	<b>0.794</b>	<b>0.792</b>	<b>0.781</b>	<b>0.769</b>	<b>0.755</b>

Table 6: Robustness to a subset of noises with detailed values.

Model	Random Latency ( $t_{\text{lag.}}$ )		
	0 ms	[100 ms, 200 ms]	[300 ms, 500 ms]
CoBEVT [1]	0.767	0.751 (1.99% ↓)	0.690 (10.06% ↓)
V2X-ViT [2]	0.772	0.758 (1.80% ↓)	0.703 (9.01% ↓)
Where2comm [3]	0.776	0.759 (2.21% ↓)	0.711 (8.42% ↓)
M2C-S (Ours)	0.776	0.765 (1.39% ↓)	0.720 (7.21% ↓)
M2C-P (Ours)	0.788	<b>0.776 (1.55% ↓)</b>	<b>0.729 (7.54% ↓)</b>
Model	Location Noise std. ( $\sigma_{\text{loc.}}$ )		
	0.0 m	[0.1 m, 0.2 m]	[0.3 m, 0.5 m]
CoBEVT [1]	0.767	0.754 (1.61% ↓)	0.682 (11.04% ↓)
V2X-ViT [2]	0.772	0.769 (0.44% ↓)	0.704 (8.81% ↓)
Where2comm [3]	0.776	0.765 (1.42% ↓)	0.697 (10.27% ↓)
M2C-S (Ours)	0.776	0.777 (0.13% ↑)	0.711 (8.30% ↓)
M2C-P (Ours)	<b>0.788</b>	<b>0.788 (0.03% ↑)</b>	<b>0.719 (8.75% ↓)</b>
Model	Heading Noise std. ( $\sigma_{\text{hdg.}}$ )		
	0.0°	[0.2°, 0.4°]	[0.6°, 1.0°]
CoBEVT [1]	0.767	0.763 (0.43% ↓)	0.719 (6.23% ↓)
V2X-ViT [2]	0.772	0.773 (0.12% ↑)	0.748 (3.17% ↓)
Where2comm [3]	0.776	0.773 (0.44% ↓)	0.745 (4.02% ↓)
M2C-S (Ours)	0.776	0.780 (0.60% ↑)	0.754 (2.79% ↓)
M2C-P (Ours)	<b>0.788</b>	<b>0.793 (0.59% ↑)</b>	<b>0.768 (2.52% ↓)</b>

## C Experiments.

### C.1 Noise Robustness.

To evaluate the robustness against noise, we train and validate models under the harsh noise setting (Sections B.4 and B.5). As shown in Table 5 with detailed values, our M2C-S and M2C-P outperform the SOTA models across all noise components. To present a detailed comparison, we divide the

noise sets into two subsets: 1) normal noise and 2) severe noise. The normal noise subset is based on the normal range defined in the work [2]. In this paper, we define a normal noise subset as  $t_{\text{lag}} \in [100 \text{ ms}, 200 \text{ ms}]$ ,  $\sigma_{\text{loc.}} \in [0.1 \text{ m}, 0.2 \text{ m}]$ , and  $\sigma_{\text{hdg.}} \in [0.2^\circ, 0.4^\circ]$ , and the severe noise subset as  $t_{\text{lag}} \in [300 \text{ ms}, 500 \text{ ms}]$ ,  $\sigma_{\text{loc.}} \in [0.3 \text{ m}, 0.5 \text{ m}]$ , and  $\sigma_{\text{hdg.}} \in [0.6^\circ, 1.0^\circ]$ . In Table 6, we evaluate performance by averaging each component in the subset.

**Normal Noise.** Under normal noise conditions, our models outperform the SOTA models. In particular, M2C-P shows the best performance, improving performance in terms of latency, localization noise, and heading noise by 2.23%, 2.56%, and 2.57% compared to the highest performance. Moreover, both M2C-S and M2C-P demonstrate the lowest sensitivity to noise. Our models exhibit performance enhancements regarding localization and heading noise, while most SOTA models show reduced performance.

**Severe Noise.** Our models outperform the SOTA models in severe noise conditions. M2C-P increases by 2.23%/2.56%/2.57% compared to the highest performance. In addition, our models show the lowest sensitivity to severe noise.

## C.2 Detection Visualization.

We visualize the detection results in the V2V and V2I scenarios, respectively. In the V2V scenario (Fig. 7), our models demonstrate robustness to occlusion. Moreover, the bounding boxes generated by our models align well with the detected objects, showing superior alignment compared to those produced by the SOTA models. In the V2I scenario (Fig. 8), our models effectively utilize sparse point clouds from the infrastructure for detection. Additionally, the predicted bounding boxes are more precise than those of the SOTA models.

## C.3 Attention Weights Visualization.

In Figure 9, we visualize additionally the attention weights in agent-wise attention of models in V2V scenario, where the brighter colors indicate the areas the ego agent focuses on. Some observations to notice are as follows: i) Our models show a clear difference between the regions that are paid attention to or not, compared to the V2X-ViT’s attention weights (Figure 9-(b)). ii) Our models have different attention tendencies. For the M2C-P in Figure 9-(d), the ego agent relies on its own confidence regions where its point clouds are dense and not occluded and also on the aux agent’s confidence regions to incorporate wide-range information. In the M2C-S in Figure 9-(c), the ego agent focuses on the areas where objects densely exist.

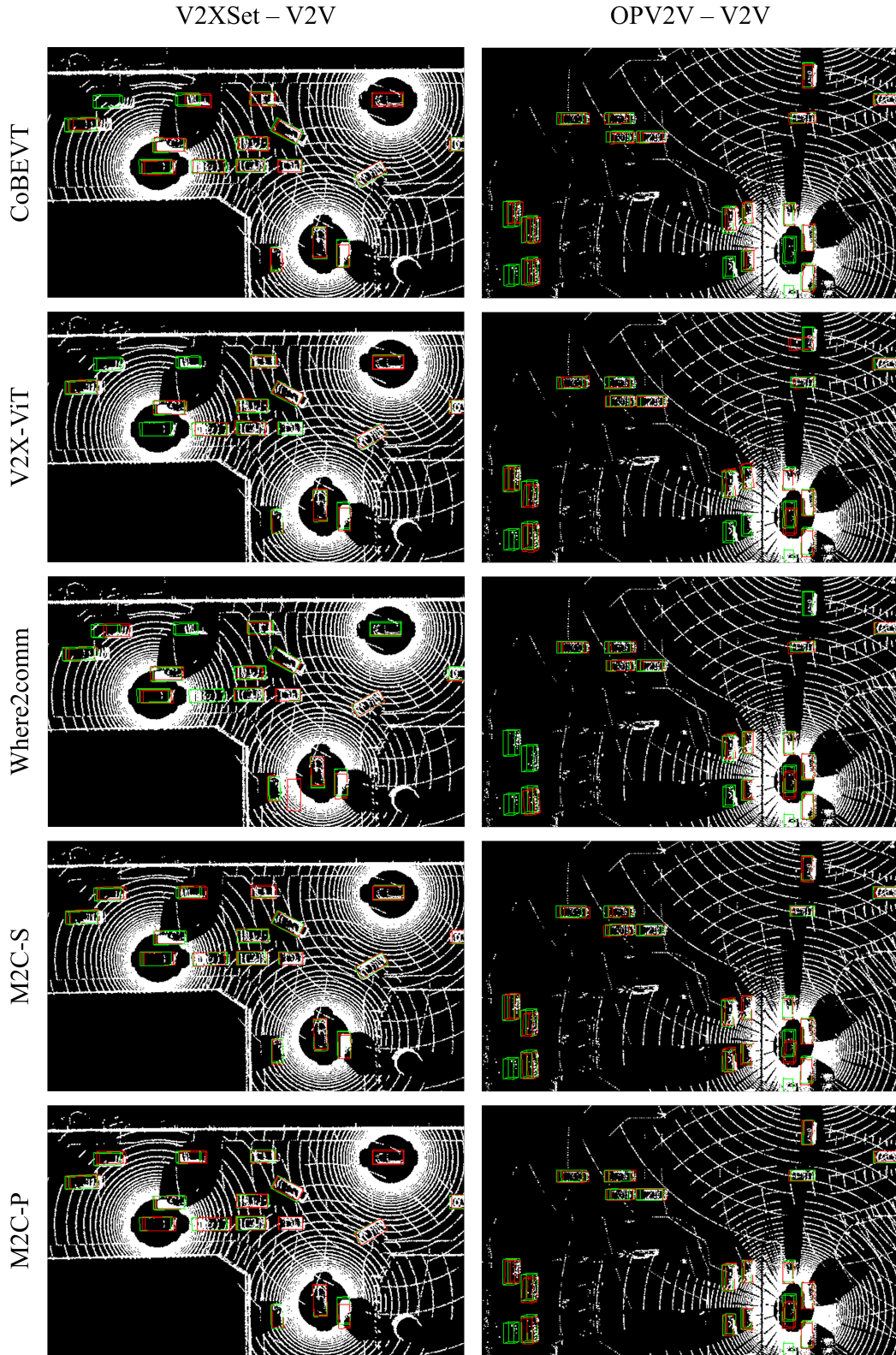


Figure 7: Detection visualization of V2V scenarios. The green bounding boxes represent the ground truth, indicating vehicles driving on the road, while the red bounding boxes denote predictions. These V2V scenarios are extracted from the V2XSet and OPV2V datasets.

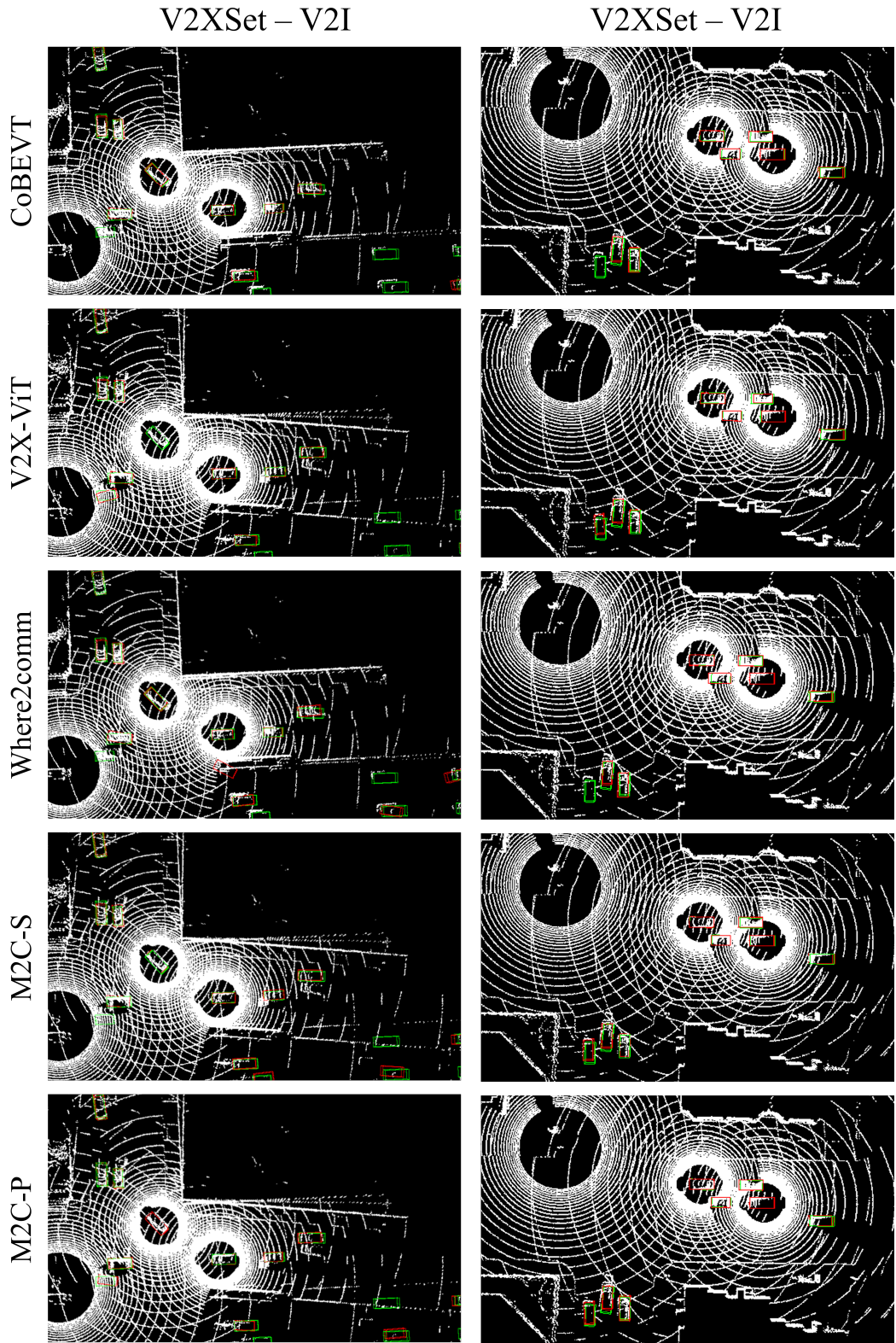


Figure 8: **Detection visualization of V2I scenarios.** The **green bounding boxes** represent the ground truth, indicating vehicles driving on the road, while the **red bounding boxes** denote predictions. These V2I scenarios are extracted from the V2XSet datasets.

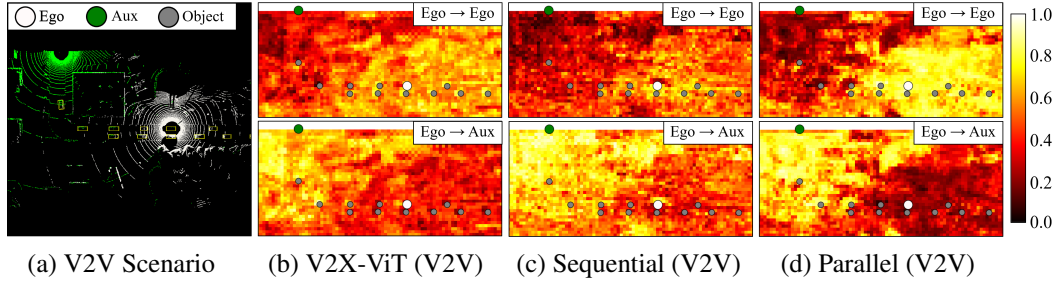


Figure 9: **Aggregated LiDAR points and attention map for V2V.** The white circle is the ego agent, and the blue and green circles are aux agents. Small grey circles are vehicles in the detection range.

## References

- [1] Runsheng Xu, Zhengzhong Tu, Hao Xiang, Wei Shao, Bolei Zhou, and Jiaqi Ma (2022) Cooperative Bird’s Eye View Semantic Segmentation with Sparse Transformers, In *Proceedings of The 6th Conference on Robot Learning (CoRL)*, pp. 989–1000.
- [2] Runsheng Xu, Hao Xiang, Zhengzhong Tu, Xin Xia, Ming-Hsuan Yang, and Jiaqi Ma, V2X-ViT: Vehicle-to-Everything Cooperative Perception with Vision Transformer, In *Proceedings of the European Conference on Computer Vision (ECCV)*, 2022.
- [3] Hu, Y., Fang, S., Lei, Z., Zhong, Y., & Chen, S. (2022). Where2comm: Communication-efficient collaborative perception via spatial confidence maps. In *Advances in neural information processing systems*, 35, 4874-4886.
- [4] Qiao, D., & Zulkernine, F. (2023). Adaptive feature fusion for cooperative perception using lidar point clouds. In *Proceedings of the IEEE/CVF winter conference on applications of computer vision*, 1186-1195.
- [5] Yang, D., Yang, K., Wang, Y., Liu, J., Xu, Z., Yin, R., ... & Zhang, L. (2024). How2comm: Communication-efficient and collaboration-pragmatic multi-agent perception. In *Advances in Neural Information Processing Systems (NeurIPS)*, 36.
- [6] Li, Y., Ren, S., Wu, P., Chen, S., Feng, C., & Zhang, W. (2021). Learning distilled collaboration graph for multi-agent perception. In *Advances in Neural Information Processing Systems (NeurIPS)*, 34, 29541-29552.
- [7] Krizhevsky, A., Sutskever, I., & Hinton, G. E. (2012). ImageNet Classification with Deep Convolutional Neural Networks. In *Advances in Neural Information Processing Systems (NeurIPS)*, 25, pp. 1097–1105.
- [8] Simonyan, K., & Zisserman, A. (2014). Very Deep Convolutional Networks for Large-Scale Image Recognition. *arXiv preprint*, arXiv:1409.1556.
- [9] He, K., Zhang, X., Ren, S., & Sun, J. (2016). Deep Residual Learning for Image Recognition. In *Proceedings of the IEEE Conference on Computer Vision and Pattern Recognition (CVPR)*, pp. 770–778.
- [10] Dosovitskiy, A., Beyer, L., Kolesnikov, A., Weissenborn, D., Zhai, X., Unterthiner, T., ... & Hounsby, N. (2020). An Image is Worth 16x16 Words: Transformers for Image Recognition at Scale. In *International Conference on Learning Representations (ICLR)*.
- [11] Liu, Z., Lin, Y., Cao, Y., Hu, H., Wei, Y., Zhang, Z., Lin, S., & Guo, B. (2021). Swin Transformer: Hierarchical Vision Transformer using Shifted Windows. In *Proceedings of the International Conference on Computer Vision (ICCV)*, pp. 10012–10022.
- [12] J. Yu et al., Pooling-based Vision Transformers: Enhancing Model Efficiency by Reducing Spatial Redundancy. In *Proceedings of the IEEE/CVF International Conference on Computer Vision*, 2021, pp. 1205-1214.
- [13] A. Hassani et al., Neighborhood Attention Transformer: Towards Efficient and Scalable Processing in Dense Prediction Tasks. In *Proceedings of the IEEE/CVF Conference on Computer Vision and Pattern Recognition*, 2023, pp. 4389-4398.
- [14] A. H. Lang et al., PointPillars: Fast Encoders for Object Detection from Point Clouds. In *Proceedings of the IEEE/CVF Conference on Computer Vision and Pattern Recognition*, 2019, pp. 12697-12705.

- [15] Y. Zhou and O. Tuzel, VoxelNet: End-to-end Learning for Point Cloud Based 3D Object Detection. In *Proceedings of the IEEE/CVF Conference on Computer Vision and Pattern Recognition*, 2018, pp. 4490-4499.
- [16] B. Graham, M. Engelcke, and L. van der Maaten, 3D Semantic Segmentation with Submanifold Sparse Convolutional Networks. In *Proceedings of the IEEE/CVF Conference on Computer Vision and Pattern Recognition*, 2018, pp. 9224-9232.
- [17] A. Hassani et al., Dilated Neighborhood Attention Transformer for Precise Multi-Scale Prediction, In *Proceedings of the IEEE/CVF International Conference on Computer Vision*, 2023, pp. 3104-3113.
- [18] R. Xu et al., OPV2V: An Open Benchmark Dataset and Fusion Pipeline for Perception with Vehicle-to-Everything Communication. In *Proceedings of the IEEE International Conference on Robotics and Automation (ICRA)*, 2021, pp. 8539-8545.
- [19] A. Dosovitskiy et al., CARLA: An Open Urban Driving Simulator. In *Proceedings of the 1st Annual Conference on Robot Learning*, 2017, pp. 1-16.
- [20] R. Xu et al., OpenCDA: A Comprehensive Framework for Testing and Benchmarking Cooperative Driving Automation. In *Proceedings of the IEEE International Conference on Intelligent Transportation Systems*, 2021, pp. 1234-1241.
- [21] I. Loshchilov and F. Hutter, Decoupled Weight Decay Regularization in Deep Learning. In *Proceedings of the International Conference on Learning Representations*, 2019.
- [22] Liang, M., Yang, B., Wang, S., & Urtasun, R. (2018). Deep continuous fusion for multi-sensor 3d object detection. In *Proceedings of the European conference on computer vision (ECCV)*. pp. 641-656.
- [23] Wang, B., Zhang, L., Wang, Z., Zhao, Y., & Zhou, T. (2023). Core: Cooperative reconstruction for multi-agent perception. In *Proceedings of the IEEE/CVF International Conference on Computer Vision*. pp. 8710-8720
- [24] Yang, K., Yang, D., Zhang, J., Li, M., Liu, Y., Liu, J., ... & Song, L. (2023). Spatio-temporal domain awareness for multi-agent collaborative perception. In *Proceedings of the IEEE/CVF International Conference on Computer Vision*. pp. 23383-23392.
- [25] Yan, Y., Mao, Y., & Li, B. (2018). Second: Sparsely embedded convolutional detection. *Sensors*, 18(10), 3337.
- [26] Piergiovanni, A. J., Kuo, W., & Angelova, A. (2023). Rethinking video vits: Sparse video tubes for joint image and video learning. In *Proceedings of the IEEE/CVF Conference on Computer Vision and Pattern Recognition* pp. 2214-2224.
- [27] Lin, T. Y., Goyal, P., Girshick, R., He, K., & Dollár, P. (2017). Focal loss for dense object detection. In *Proceedings of the IEEE International Conference on Computer Vision (ICCV)* pp. 2980-2988.
- [28] Shi, G., Li, R., & Ma, C. (2022, October). Pillarnet: Real-time and high-performance pillar-based 3d object detection. In *Proceeding of the European Conference on Computer Vision (ECCV)* pp. 35-52. Cham: Springer Nature Switzerland.
- [29] Yin, T., Zhou, X., & Krahenbuhl, P. (2021). Center-based 3d object detection and tracking. In *Proceedings of the IEEE/CVF Conference on Computer Vision and pattern recognition (CVPR)* pp. 11784-11793.
- [30] Zhu, B., Jiang, Z., Zhou, X., Li, Z., & Yu, G. (2019). Class-balanced grouping and sampling for point cloud 3d object detection. *arXiv preprint*, arXiv:1908.09492.
- [31] Berrada, L., Zisserman, A., & Kumar, M. P. (2018). Smooth loss functions for deep top-k classification. *arXiv preprint*, arXiv:1802.07595.
- [32] Xu, R., Li, J., Dong, X., Yu, H., & Ma, J. (2023, May). Bridging the domain gap for multi-agent perception. In *2023 IEEE International Conference on Robotics and Automation (ICRA)*, pp. 6035-6042.
- [33] Chen, Z., Shi, Y., & Jia, J. (2023). TransIFF: An Instance-Level Feature Fusion Framework for Vehicle-Infrastructure Cooperative 3D Detection with Transformers. In *Proceedings of the IEEE/CVF International Conference on Computer Vision*, pp. 18205-18214.
- [34] Loshchilov, I., & Hutter, F. (2016). Sgdr: Stochastic gradient descent with warm restarts. *arXiv preprint* arXiv:1608.03983.